Supporting Information

Silicon Monophosphide with Controlled Size and Crystallinity for Enhanced Lithium Anodic Performance

Huanhuan Yang, Binlu Yu, Shuang Gu, Hao Huang, Yanli Zhang, Danni Liu, Xue Zhang, Yihong Kang, Jiahong Wang, Paul K. Chu, and Xue-Feng Yu**

Experimental Section

Materials: The silicon powder (200 mesh) was purchased from Sinopharm Chemical Reagent Co., Ltd. and sulphur (99%) was obtained from Alfa Aesar. The red phosphorus powder (99.999%), iodine (99.99%), and *N*-methylpyrrolidone (NMP, 99.99%) were bought from Aladdin. All the chemicals were used as received without further purification.

Crystal growth

Growth of HT-SiPs: The HT-SiPs were synthesized by a high temperature chemical vapor transport (CVT) method (1060-1030 ℃). The silicon and red phosphorus powders were used as raw materials and iodine was added as a transporting agent for the growth of the HT-SiPs. 600 mg of a stoichiometric mixture of silicon and phosphorus (1:1) and 10 mg of iodine were sealed in a quartz ampoule with a length of 20 cm, inner diameter of 11 mm, and thickness of 2 mm. After sealing under a pressure of 1×10^{-1} Pa, the ampoule was placed in a horizontal two-zone furnace. The two zones were slowly heated to 1060 ℃ (T_1, source) and 1030 ℃ (T_2, empty side) at a rate of 10 ℃/min and kept for 4 days. The HT-SiPs crystals were obtained from the high temperature zone. The product was rinsed with acetone and ethanol and dried.

Growth of LT-SiPs: The LT-SiPs were grown by CVT at a lower temperature. 600 mg of a stoichiometric mixture of silicon and phosphorus (1:1) and 10 mg of iodine were sealed in a quartz ampoule. The horizontal two-zone furnace was heated from room temperature to 800

℃ (T_1, source) and 900 ℃ (T_2, sink) and kept for 4 days. After natural cooling, the fibrous LT-SiPs were obtained from the high temperature zone of the ampoule. The product was washed and dried.

Growth of bulk SiPs: The bulk SiPs were prepared by the sulfur-assisted CVT method. 600 mg of the stoichiometric mixture of silicon and phosphorus (1:1), 10 mg of iodine, and 15 mg of sulfur (S) were put into a quartz ampoule. The horizontal two-zone furnace was heated to 1060 ℃ (T_1, source) and 1030 ℃ (T_2, sink) for 4 days after which the ampoule cooled naturally to room temperature. The brick-shaped bulk SiPs crystals were obtained from the low temperature zone. The product was washed and dried.

Characterization: The crystal structure was determined by X-ray diffraction (Rigaku Smartlab 3kW X-ray diffractometer with Cu Kα radiation (λ = 1.54056 Å)) and the Raman scattering spectra were acquired from the Horiba Jobin Yvon LabRam HR800 high resolution confocal Raman microscope equipped with a laser of 633 nm. Atomic force microscopy (AFM) was performed on the Cypher S AFM (Asylum Research, USA). The morphology of the samples was examined by scanning electron microscopy (Zeiss Supra 55, Germany). Transmission electron microscopy was carried out on the JEOL JEM-3100F 300 kV. Selected-area electron di□raction (SAED), high-resolution TEM (HR-TEM), and energy-dispersive X-ray spectroscopy (EDS) were conducted. The binding energies were determined by XPS (Thermo Fisher ESCALAB 250Xi XPS). Prior to TEM examination of the SiP electrode after de-lithiation, the sample was scraped from the Cu substrate, dispersed in anhydrous ethanol, and dropped onto a carbon-coated TEM grid.

Electrochemical characterization: The electrodes were composed of 70 wt% SiP, 20 wt% acetylene black, and 10 wt% PVDF binder. The composite was dispersed in *N*-methylpyrrolidone (NMP) and ground into a homogeneous paste, blade-cast onto a copper foil (diameter 12 mm, thickness 15 μm), and dried at 120 ℃ for 10 h under vacuum. The mass loading of the active materials was about 1.0 mg cm^{-2}. In the electrochemical measurement,

CR2032 coin-type half-cells were assembled with a counter electrode of lithium metal disk (14 mm in diameter), working electrode of SiP, polypropylene separators (16 mm in diameter), as well as 25 μL of electrolyte (1 M $LiPF_6$ in a mixture of dimethyl carbonate (DMC), ethylene carbonate (EC) and diethyl carbonate (DEC) (DMC:EC:DEC=1:1:1,v/v/v)). The charging/discharging test was conducted on a Neware battery testing system in the constant current mode. Galvanostatic cycling was conducted between 0.01 and 1.5 V *vs* Li/Li^+ at a current density of 100 mA g^{-1}. To assess the rate capability, different current densities in the range of 100–5000 mA g^{-1} were applied and the specific capacity and current density were calculated based on the mass of SiP. Cyclic voltammetry (CV) was carried out on the CHI 760E instrument (CH Instruments, Inc., Shanghai) at a scanning rate of 0.1 mV s^{-1} in the range of 0.01-1.5 V. Electrochemical impedance spectroscopy (EIS) was performed at the open-circuit voltage vs Li^+/Li with an AC amplitude of 5 mV over the frequencies from 10^5 Hz to 0.1 Hz on the same electrochemical workstation at ambient temperature. The galvanostatic intermittent titration measurement was carried out with a pulse current of 50 mA g^{-1} for 10 min and resting for 10 min.

1. The grain size calculated by Scherrer equation:

$$D_{hkl} = \frac{K\gamma}{B\cos\theta} \quad (1)$$

Where K is Scherrer's constant (K=0.89), γ is the X-ray wavelength ($\gamma = 0.154056\ nm$), B is the full width at half maximum (FWHM) of the measured diffraction peak (unit: rad), θ is the Bragg diffraction angle (unit: degree), D_{hkl} is the average thickness of crystal grains perpendicular to the crystal plane direction (nm).

2. Lithium diffusion coefficient calculated by Electrochemical impedance spectroscopy:

The lithium diffusion coefficient (D_{Li^+}) is calculated in the low frequency according to the following equations:

Radial frequency: $\omega = 2\pi f$ (2)

Warburg impedance: $Z_W = \sigma(\omega)^{-\frac{1}{2}}(1-j)$ (3)

Lithium diffusion coefficient (D_{Li^+}): $D_{Li^+} = \frac{R^2T^2}{2S^2n^4F^4C_{Li^+}^2\sigma^2}$, (4)

where σ is the Warburg coefficient, ω is the radial frequency, R is the gas phase constant, T is the absolute temperature, S is the surface area of the electrode, n is number of electrons transferred in the oxidation or reduction electrochemical reaction, F is Faraday's constant, and C_{Li^+} is the concentration of lithium ion in the solid phase of the electrode. σ can be acquired from the linear fitting of Z' versus $\omega^{-1/2}$ (**Fig. S7**).

3. GITT test is a reliable and effective method for testing lithium ion diffusivity.

The lithium ion diffusivity *(D_{Li^+})* can be obtained by the following equation: [1]

$$D_{Li^+} = \frac{4}{\pi\tau}\left(\frac{m_B V_m}{M_B S}\right)^2\left(\frac{\Delta E_s}{\Delta E_t}\right)^2, \quad (5)$$

where τ is the current pulse time, m_B is the mass of the electrode, V_m and M_B are the molar volume and molar mass of the electrode, respectively, S is the electrode/electrolyte contact area, ΔE_s is the steady-state voltage change due to the current pulse, and ΔE_t is the voltage change during the constant current pulse eliminating the iR drop.

Supporting Figures

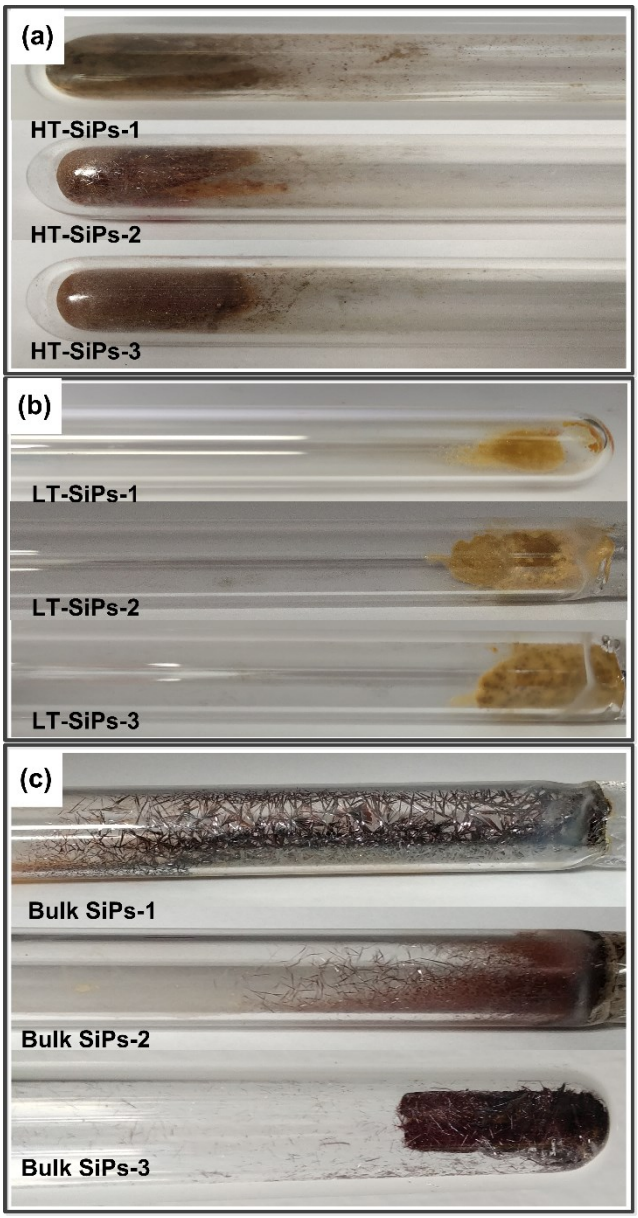

Fig. S1 Photographs of the quartz tube for three samples prepared by three techniques.

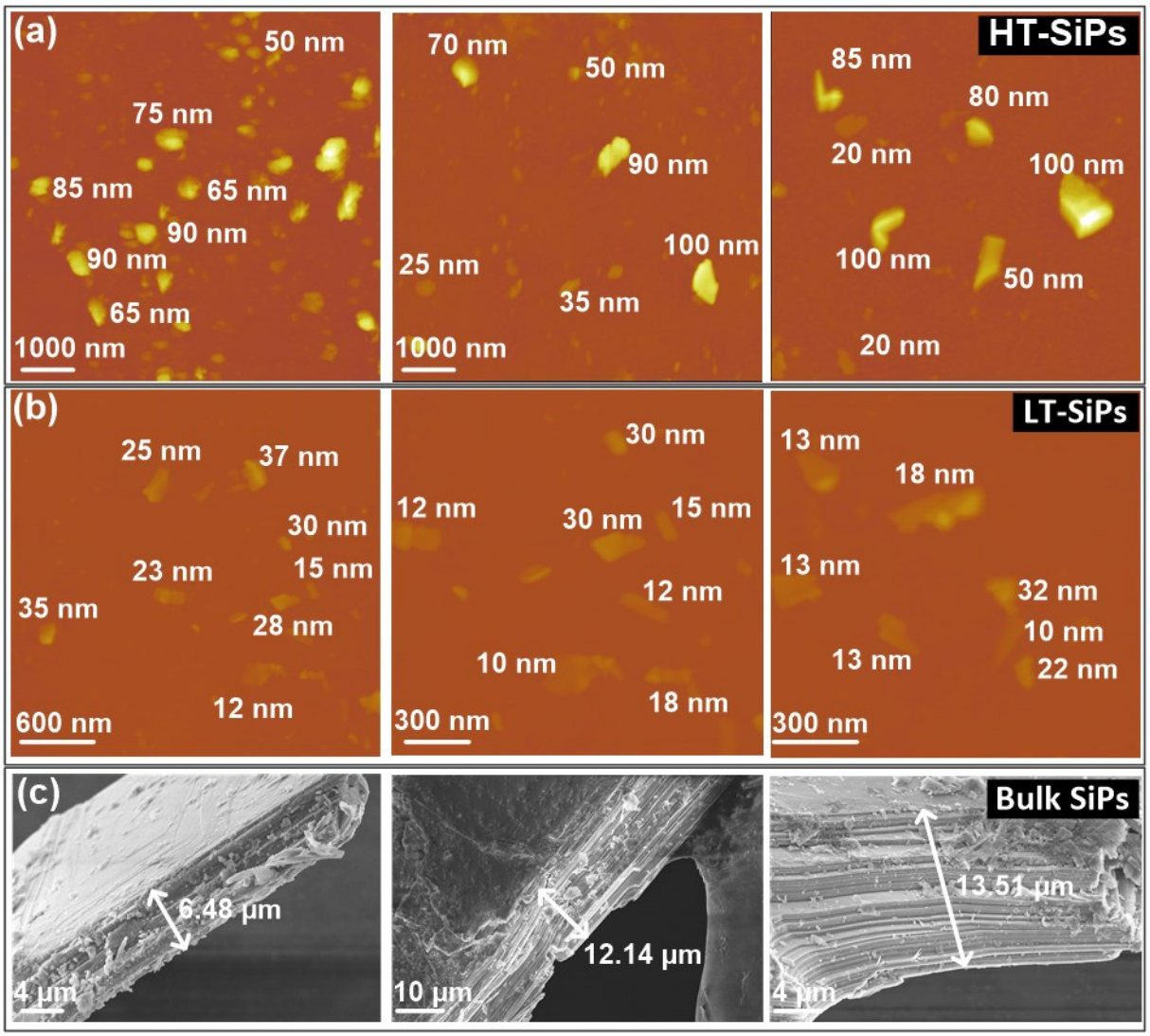

Fig. S2 AFM images of (a) HT-SiPs and (b) LT-SiPs, SEM images of (c) bulk SiPs for width data.

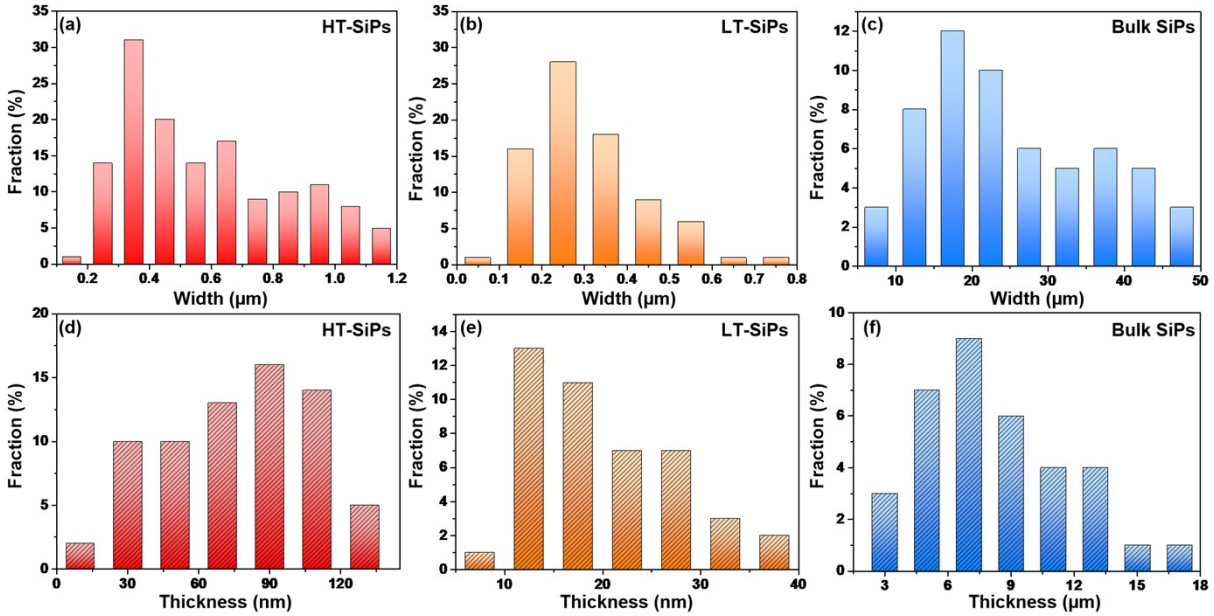

Fig. S3 Width and thickness distribution histograms of different SiPs (at least 100 sheets were measured)

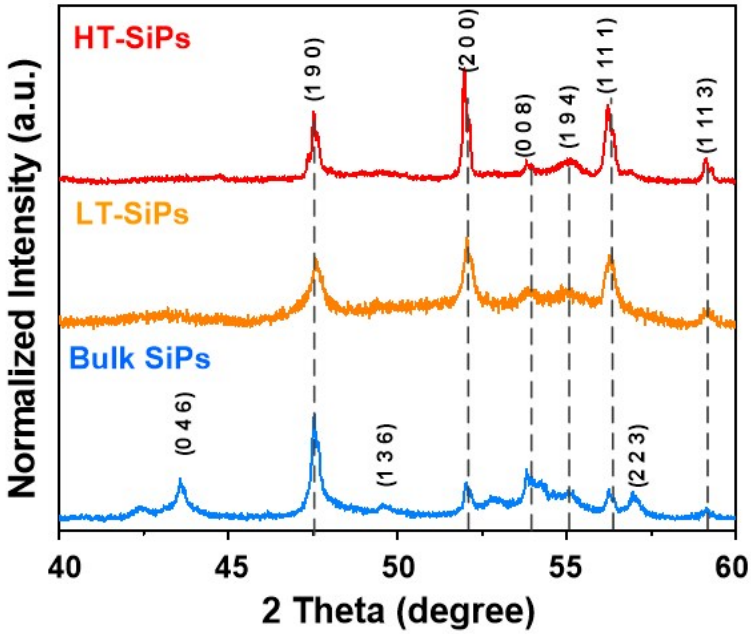

Fig. S4 XRD pattern between 40° and 60° of three samples.

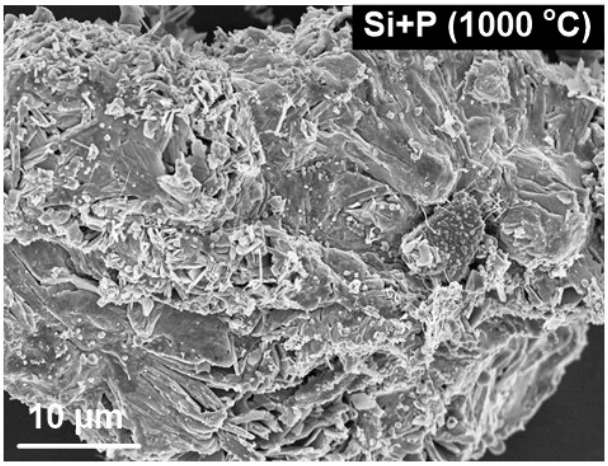

Fig. S5 SEM image of Si+P (1000 ℃) without transport agents iodine.

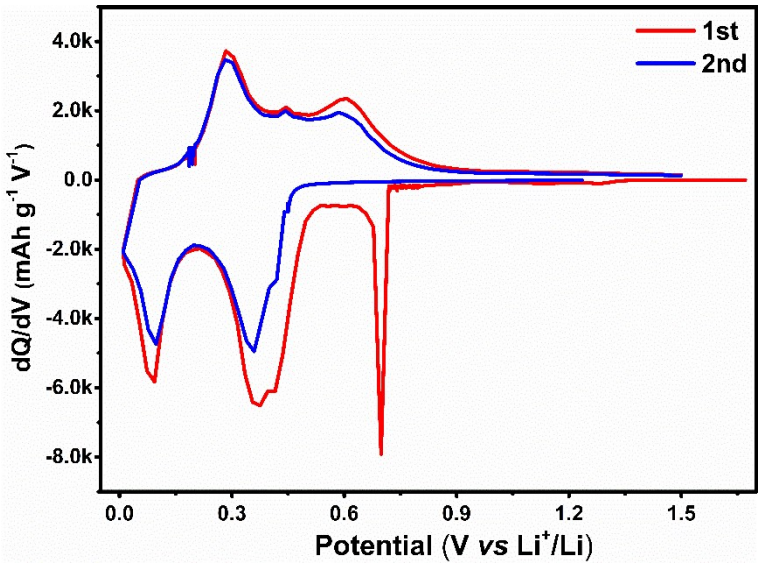

Fig. S6 Differental capacity plot (DCP) of SiPs during the first and second cycles.

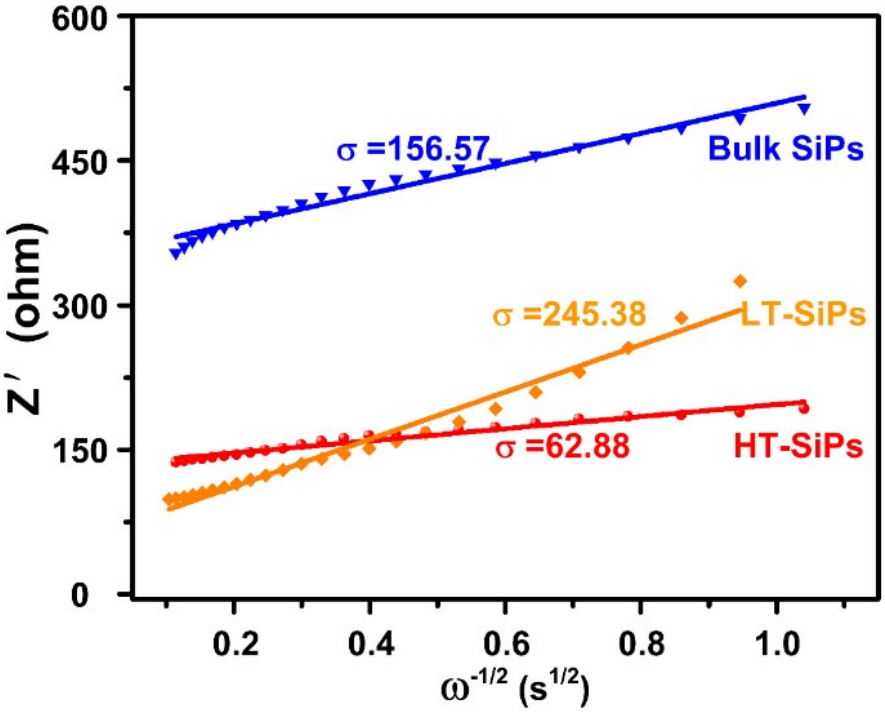

Fig. S7 Linear fits of the fresh cell of HT-SiPs, LT-SiPs and bulk SiPs.

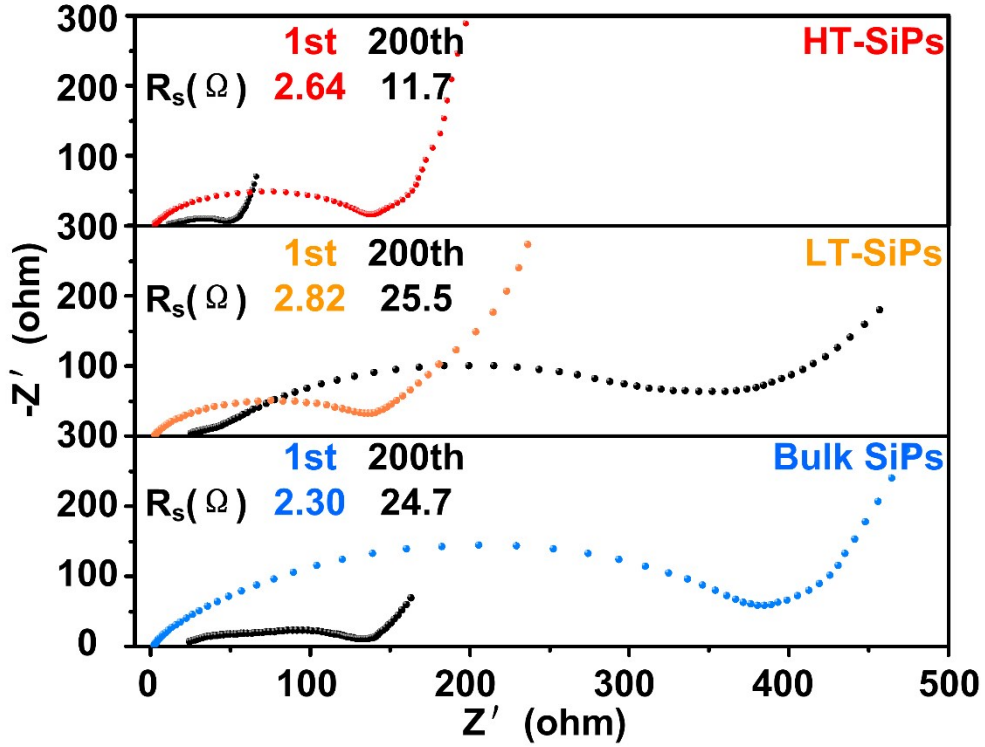

Fig. S8 EIS plots of the HT-SiPs, LT-SiPs and bulk SiPs fresh cell and after 200 cycles (black dots).

The EIS plots in **Fig. 3b** are fitted with the model of R1(CPE1-R2)(CPE2-R3)W2, where the contributing parameters are defined as follows [6]: R1 is the resistance of bulk electrolyte (R_s) corresponding to the horizontal axis intercept in the high-frequency region, R_{ct} (R_{ct} = R2 + R3) represents the charge transfer resistance between the electrolyte and electrode, and CPE stands for the constant phase element phase elements in the circuit.

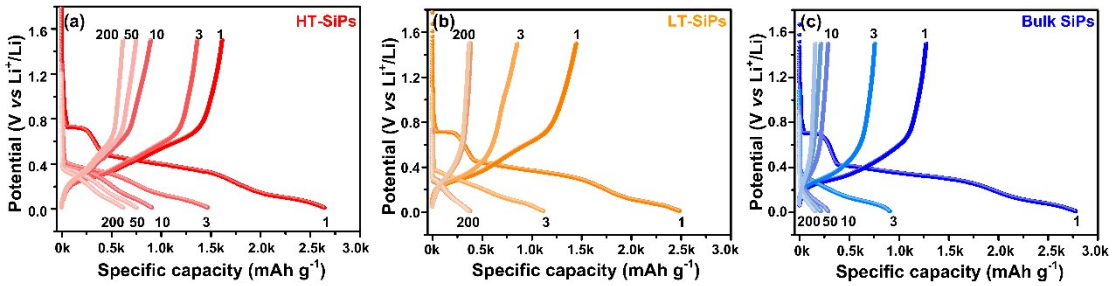

Fig. S9 Galvanostatic charging/discharging profiles of (a) HT-SiPs, (b) LT-SiPs, and (c) bulk SiPs for different cycles at a current density of 100 mA g^{-1} in the potential range between 0 and 1.5 V.

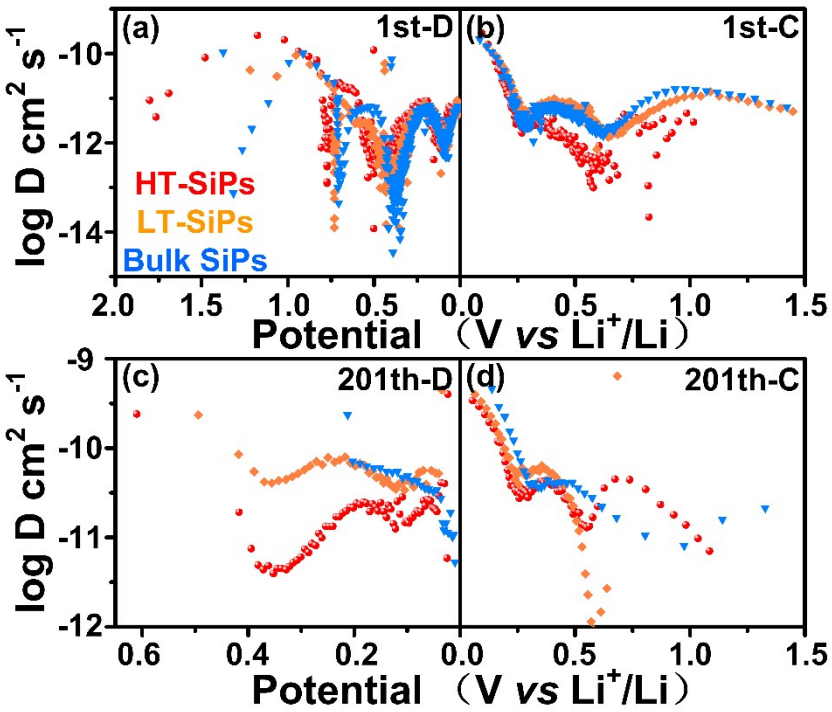

Fig. S10 Comparison of D_{in}- $_{Li}^{+}$ and D_{ex}- $_{Li}^{+}$ in the first cycle for (a, b) discharging and, charging and (c, d) 201st cycle of HT-SiPs, LT-SiPs and bulk SiPs electrodes.

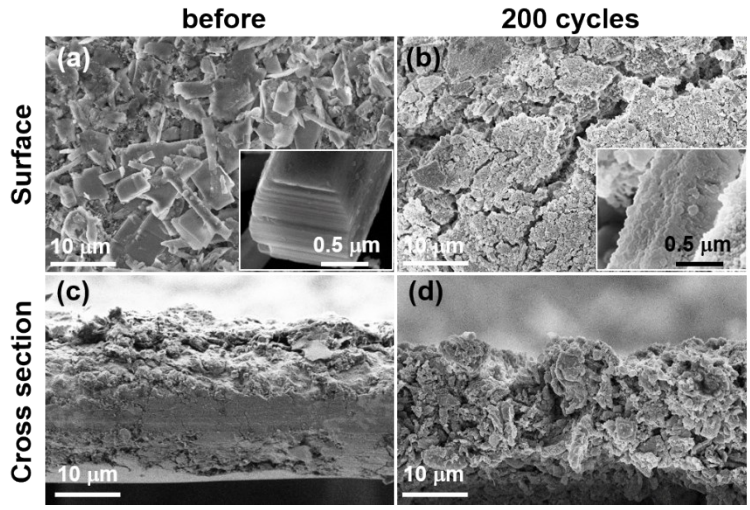

Fig. S11 SEM images of HT-SiPs electrodes: (a, b) Before cycling and after 200 cycles with the insets showing the enlarged images of the HT-SiPs nano-belts and layers pulverized after 80 cycles; (c, d) Cross section of HT-SiPs electrodes before cycling and after 200 cycles.

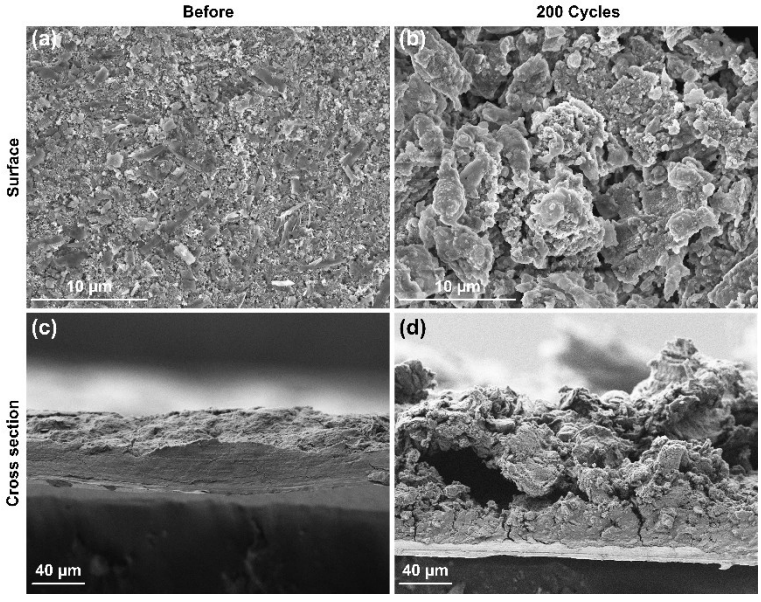

Fig. S12 SEM images of LT-SiPs electrodes: (a, b) Before cycling and after 200 cycles; (c, d) Cross section of LT-SiPs electrodes before cycling and after 200 cycles.

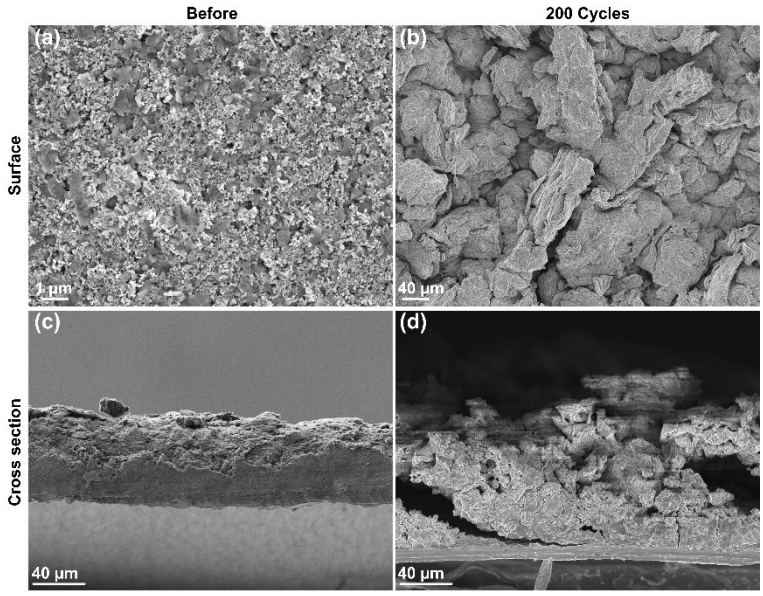

Fig. S13 SEM images of bulk SiPs electrodes: (a, b) Before cycling and after 200 cycles; (c, d) Cross section of bulk SiPs electrodes before cycling and after 200 cycles.

As shown in **Fig. S11a, S12a and S13a**, the belts are scattered in the field of vision and exhibit a distinct multi-layered structure before cycles. After continuous charging/discharging for 200 cycles, the layered structures expand and finally pulverize into particles as shown in **Fig. S11b, S12b and S13b**. By comparing the morphology of the HT-SiPs of the cross sections (**Fig. S11c and S11d**), the electrode materials are gradually separated from the copper collector until they are completely detached from the collector surface. There are different degrees of cracks in the cross section of LT-SiPs and bulk SiPs (**Fig. S12c, S12d, S13c and S13d**). The capacity is directly related to the state of the electrode material, which is also one of the reasons for the excellent performance of HT-SiPs. And, pulverization and expansion of the materials may be a major cause for capacity fading.

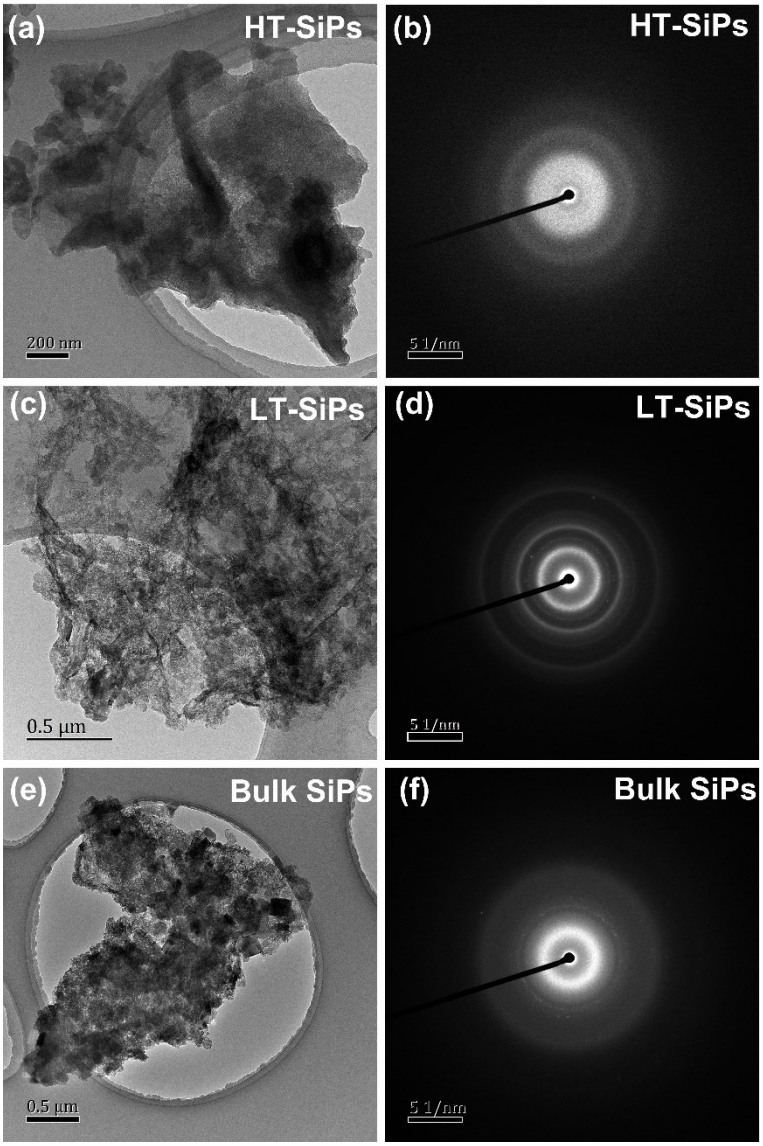

Fig. S14 Three electrodes after 200 cycles: (a, c, e) TEM images and (b, d, f) SADE patterns of HT-SiPs, LT-SiPs and bulk SiPs.

The TEM and SADE images (**Fig. S14**) of the HT-SiPs, LT-SiPs and bulk SiPs electrodes after 200 cycles show amorphization and polycrystalline diffraction rings, which reveal that the original structure cannot be maintained after charging/discharging. The possible reason for the destruction of the crystal structure is that the lithium ions are inserted between the layers, causing the lattice to expand and the lattice spacing is no longer fixed. In contrast, HT-SiPs has a relatively complete structure after the same cycles.

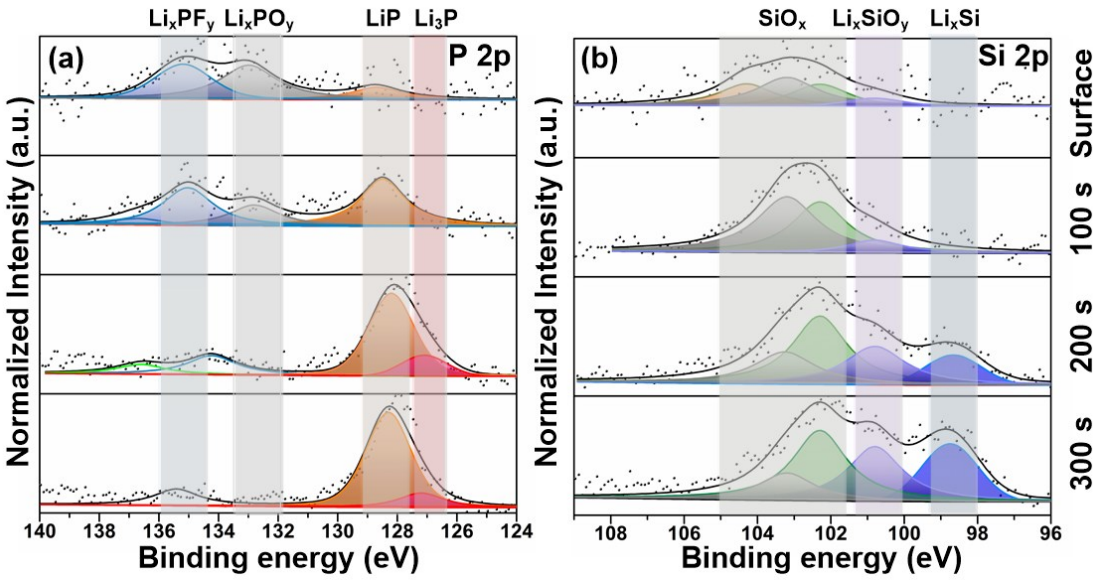

Fig. S15 *Ex situ* XPS of the HT-SiPs electrode after 35 cycles: (a) P 2p spectra and (b) Si 2p spectra before and after etching 100 s (~50 nm), 200 s (~100 nm) and 300 s (~150 nm).

The XPS results of HT-SiPs after 35 cycles with sputtering time are shown in **Fig. S15**. The signal at around 136.7 eV is caused by PF_x incomplete electrolyte removal, whereas that at around 132.8 eV is allocated to P–O species such as Li_xPO_y–like compounds arising from electrolyte decomposition of carbonate-based solvent [7]. The signals around 128.7 eV indicate the formation of a thin LiP layer. After Ar^+ ion etching for 100 s to remove the upper layer, the LiP concentration increases and Li_xPO_y and PF_x spread more deeply into the layer. After sputtering for 200 s (about 100 nm into the layer), the proportion of P-O and PF_x drops sharply but Li_3P (around 127.2 eV) becomes visible[2]. Similarly, SiO_x and SiO_y (about 103.4 and 102.2 eV) as well as Li_xSiO_y (about 100.8 eV) are detected from the "surface". With further etching, Li_xSiO_y increases further and a small amount of Li_xSi is observed (97.8 eV).

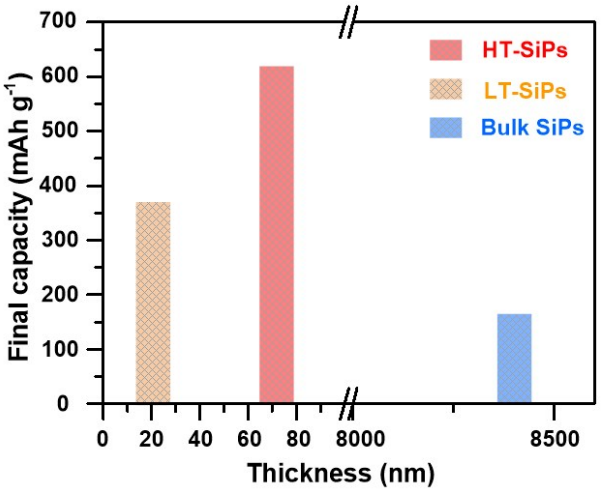

Fig. S16 The relationship between the thickness of SiPs and their final capacity.

Supporting Tables

Table S1. Full width at half maximum (FWHM) ang grain size corresponding to different diffraction peaks of HT-SiPs, LT-SiPs and bulk SiPs.

Sample	2Theta (13 °) (002)		2Theta (21.3 °) (023)	
	FWHM	Size(nm)	FWHM	Size(nm)
Si+P (1000 ℃)	0.0862	96.9	1.05	8.0
LT-SiPs (800-900 ℃)	0.1471	56.8	0.9177	9.2
HT-SiPs (1060-1030 ℃)	0.095	87.6	0.93	9.1
Bulk SiPs (1060-1030 ℃)	0.0623	134.0	0.112	75.6

Table S2. Lithium ion diffusion coefficients in different materials obtained by different techniques.

Material	Diffusion coefficient ($cm^2\ s^{-1}$)	Technique	Reference
graphite	$1.03\times10^{-12} – 9.30\times10^{-14}$ 2.27×10^{-13}	PITT Warburg impedance	(8)
monocrystalline silicon Nanosized amorphous Si	1.13×10^{-16} (at 255K) 1×10^{-13} (at 498K)	LA-ICP-MS and ToF-SIMS neutron reflectometry and SIMS	(9) (10)
silicon monophosphide	$8.61\times10^{-10} – 2.31\times10^{-13}$ 4.226×10^{-15}	GITT Warburg impedance	In this work

PITT: Potential Intermittent Tiration Technique;

ToF-SIMS: secondary ion mass spectroscopy with a reflector time-of-flight detector;

SIMS: secondary ion mass spectroscopy;

GITT: Galvanostatic Intermittent Titration Technique;

Table S3. Comparison of the electrochemical properties of three samples for different cycles.

Samples / cycle	Discharge capacity (mAh g^{-1})		
	HT-SiPs	LT-SiPs	Bulk SiPs
1st	2644	2485	2778
3rd	1468	1116	910
10th	908	380	290
50th	747	374	217
200th	615	365	160

Table S4. Comparison of the capacities for different cycles with other reported SiP_x in LIBs.

material	Current density (mA g^{-1})	Potential range (V)	Capacity (mAh g^{-1})	ICE	Ref.
SiP_2	50	0.01-1.2	200 (50th cycle)	65%	(2)
SiP_2	148	0.01-2.0	750 (35th cycle)	75%	(3)
SiP_2	149	0.01-1.5	980 (35th cycle)	84%	(4)
SiP	100	0.01-1.2	550 (50th cycle)	32%	(5)
SiP	100	0.01-1.5	747 (50th cycle)	61%	This work

References

(1) C. Li, S. Wang, X. Zhang, N. Jia, T. Yu, M. Zhu, D. Liu and X. Tao, *CrystEngComm*, 2017, **19**, 6986-6991.

(2) R. Reinhold, U. Stoeck, H. J. Grafe, D. Mikhailova, T. Jaumann, S. Oswald, S. Kaskel, and L. Giebeler, *ACS Appl. Mater. Interfaces*, 2018, **10**, 7096-7106.

(3) G. Coquil, B. Fraisse, N. Dupré and L. Monconduit, *ACS Appl. Energ. Mater.*, 2018, **1**, 3778-3789.

(4) D. Duveau, S. S. Israel, J. Fullenwarth, F. Cunin and L. Monconduit, *J. Mater. Chem. A*, 2016, **4**, 3228-3232.

(5) R. Reinhold, D. Mikhailova, T. Gemming, A. B. Missyul, C. Nowka, S. Kaskel and L. Giebeler, *J. Mater. Chem. A*, 2018, **6**, 19974-19978.

(6) X. Liu, G. B. Xu, T. T. Cheng, L. W. Yang and J. X. Cao, *ChemElectroChem*, 2020, **7**, 846-854.

(7) Q. Li, X. Liu, X. Han, Y. Xiang, G. Zhong, J. Wang, B. Zheng, J. Zhou and Y. Yang, *ACS Appl. Mater. Interfaces,* 2019, **11**, 14066-14075.

(8) P. Yu, B. N. Popov, J. A. Ritter and R. E. White, *J. Electrochem. Soc.*, 1999, **146**, 8-14.

(9) R. Janski, M. Fugger, M. Sternad and M. Wilkening, *ECS Trans.*, 2014, **62**, 247-253.

(10) E. Hüger, L. Dörrer, J. Rahn, T. Panzner, J. Stahn, G. Lilienkamp and H. Schmidt, *Nano Lett.*, 2013, **13**, 1237-1244.